A 3D flow visualization in evaporation of water from a meniscus at low pressures

Mohammad Amin Kazemi[1,2], Janet A. W. Elliott[2] and David Nobes[1]*

[1]Optical Diagnostic Group, Department of Mechanical Engineering,
[2]Department of Chemical and Materials Engineering
University of Alberta, Edmonton, Canada T6G 2G8
*corresponding author: david.nobes@ualberta.ca

Abstract Evaporation of a liquid from a meniscus has been observed to generate vortical motion and instabilities both on the interface and in the bulk liquid. The aim of this work is to develop and demonstrate an automated scanning particle image velocimetry (PIV) system to visualize and quantify the time-resolved three-dimensional evaporation-driven velocity field inside the bulk liquid. The evaporating liquid is deionized water which forms a meniscus in a rectangular cross section (10mm x 4mm) quartz cuvette. In preliminary experiments, the three-dimensional velocity and vorticity fields revealed the existence of a large doughnut shape convection pattern in the bulk liquid and also a very small vortex rotating in the opposite direction close to the liquid–vapor interface. Such a detailed 3D observation of the flow field can lead to new understanding of the mechanisms of energy transport to the interface during evaporation of liquids, which has been the subject of intense study for many years.

Keywords: Evaporation driven flow, thermocapillary flow, vortex flow, PIV

1 Introduction

The instabilities in an evaporating liquid play a significant role in many areas, including crystallization [1,2], heat pipe cooling [3-5], particle self-assembly on surfaces [6,7], welding [8,9] and spray cooling [10]. The mechanisms that generate these instabilities have been the subject of several studies since the seminal work of Bénard [11] who observed a convective pattern inside an evaporating thin liquid film with a free upper surface which was heated from the bottom. This observation, which was attributed to the density variation inside the liquid, was the direct motivation of other experimental, analytical, and numerical studies afterward. However, in the 1950s Block [12] and Pearson [13] showed that the instabilities in Bénard's experiment were not due to the variation in liquid density, but were created as a result of surface temperature gradients. They explained that the surface temperature gradient would create a surface tension gradient along the interface, which in turn would lead to bulk oscillatory instabilities.

Thermocapillary convection in the liquid during evaporation plays a major role in enhancement of heat and mass transfer across the interface. In a set of experiments on the evaporation of pure water into its vapor in a stainless-steel funnel [14], heat transfer analysis near the interface revealed that the energy transport by thermocapillary convection in the bulk liquid provided as much as 50 % of the required energy for evaporation, while the rest was supplied through conduction in the bulk liquid and vapor phases. In another similar study on evaporation of a sessile water droplet on a copper substrate [15] thermocapillary convection in the liquid was shown to supply up to 98 % of the energy required for evaporation in certain cases. Therefore, a good understanding of the flow field within the liquid in evaporation experiments would be beneficial for practical improvements and optimal design.

Investigation of the velocity field during liquid evaporation has been carried out by some researchers. In the simplest case, Ward and Duan [14] measured the tangential component of the velocity close to the interface during evaporation of pure water by measuring the deflection of an elastic probe. They assumed that the velocity is uniform on the interface and used this value to perform an energy balance across the interface. Song and Nobes [16] measured two components of the velocity field during the evaporation of pure water in a rectangular cuvette using particle image velocimetry (PIV). They performed the measurements only on the centre plane and noticed two symmetric outward vortices below the interface. As they had been able to remove buoyancy effects by controlling the temperature, they concluded that the motion was a result of the Marangoni effect. Babaie et al. [17] investigated the evaporation of a polymer solution inside a square microliter cavity using PIV to measure two components of the velocity field inside the cavity. They observed differently shaped vortices in different experiments and concluded that the sizes of the vortices were strongly dependent on the geometry and viscosity of the fluid. Using fluorescent dye, they could also determine the polymer concentration distribution in the solution during evaporation. Thokchom et al. [18,19] presented the two-dimensional (2D) velocity field in an evaporating droplet. To avoid image corrections due to the droplet curvature, they used a confined 2D droplet instead of a 3D droplet and applied planar 2D PIV to obtain the two components of the velocity. They observed two outward vortices in the droplet as a result of both Marangoni and buoyancy effects which was in agreement with their numerical simulation. Buffone et al. [20] studied the thermocapillary convection generated by an evaporating meniscus in a microchannel. They visualized the flow pattern in two dimensions using µ-PIV. In the case of vertical microchannels, they observed two symmetric vortices below the interface. However, when the microchannel was horizontally oriented, only one large vortex was observed. They attributed all of these vortices to the Marangoni effect. Dehavaleswarapu et al. [21] performed 2D PIV to observe the flow field inside the liquid during evaporation of methanol from a meniscus in differently sized microtubes. In order to get a better understanding of the velocity field, they conducted PIV at three equidistant parallel planes in the tubular microchannel. Although this measurement helps to guide a better understanding of the 3D flow in the channel, the complete velocity field in the entire geometry which includes the three components of the velocity was still undefined. Minetti and Buffone [22] used a digital holographic microscopy (DHM) method to trace the 3D trajectory of individual tracer particles in an evaporating meniscus of ethanol. The 3D trajectories of the particles revealed the existence of a periodic oscillatory motion near the evaporating meniscus.

Although 2D velocity measurement in evaporating liquids has been studied by a number of researchers, detailed investigation of the three-dimensional velocity profiles in an evaporating liquid is still lacking. There are several approaches that have been applied to measure velocity components in 3D, such as defocusing PIV, multi-view PIV, holographic PIV, and scanning PIV. A detailed overview of the various 3D volumetric PIV techniques and the advantage of each method are discussed by Qi et al. [23]. The objective of this work is to develop and demonstrate an automated scanning PIV system and fully 3D measurement technique which can quantify the three components of velocity throughout the volume of an evaporating liquid. In the scanning PIV technique, oscillating optics are used to generate a planar laser sheet which scans the whole or a portion of the volume at a high frequency. The set of images, which are captured using a single camera at a fixed position, is then reconstructed to determine the position of the particles and to calculate the three components of the velocity in 3D.

2 Experimental Apparatus and Methods for PIV Experiments

The experimental setup to investigate the velocity field in an evaporating liquid consists mainly of three basic subsystems including the imaging system, the illumination system and the vacuum chamber system. The arrangement of these components is schematically illustrated in Fig. 1. A quartz cuvette (9F-Q-10, Strana Cells) with an internal dimension of 4 mm × 10 mm and a height of 45 mm was used as the liquid container. The walls and the base of the purchased cuvette were polished and were made extremely flat by the manufacturer which makes the cuvette suitable for laser and imaging techniques. Before each experiment, the cuvette was cleaned gently with detergent powder (Alconox, Inc., NY, USA) and then rinsed with a jet of deionized water five times lasting 10 s each. The experimental liquid was distilled and deionized water with a resistivity of 18.0 MΩ cm which was prepared using a water deionization system (D4641-Barnstead). To visualize and monitor the flow characteristics the water was seeded with 2.0 µm fluorescent particles (Fluoro-Max R0200, Thermo Scientific). To prepare the suspension for imaging purposes, one drop of high-concentration suspension was added to 40 ml of deionized water and gently mixed to achieve a uniform suspension. In order to prevent the formation of bubbles during the experiment, the suspension was degassed for 15 minutes by decreasing the pressure gradually. The cuvette was then situated in the vacuum chamber (CU6-0275, Kurt J. Lesker) which was connected to a vacuum pump. To control the pressure within the vacuum chamber, an angle valve was installed between the pump and the chamber. The pressure inside the chamber was measured using a pressure transducer (PX419-005A5V, OMEGA) which was situated at the top of the vacuum chamber. The temperature at the bottom of the cuvette was controlled using a thermoelectric cooling device (TEC, CP-031, TE Technology) and maintained at 4 °C. Water at this temperature is at its maximum density. This ensures that no buoyancy drive flow is present in the system.

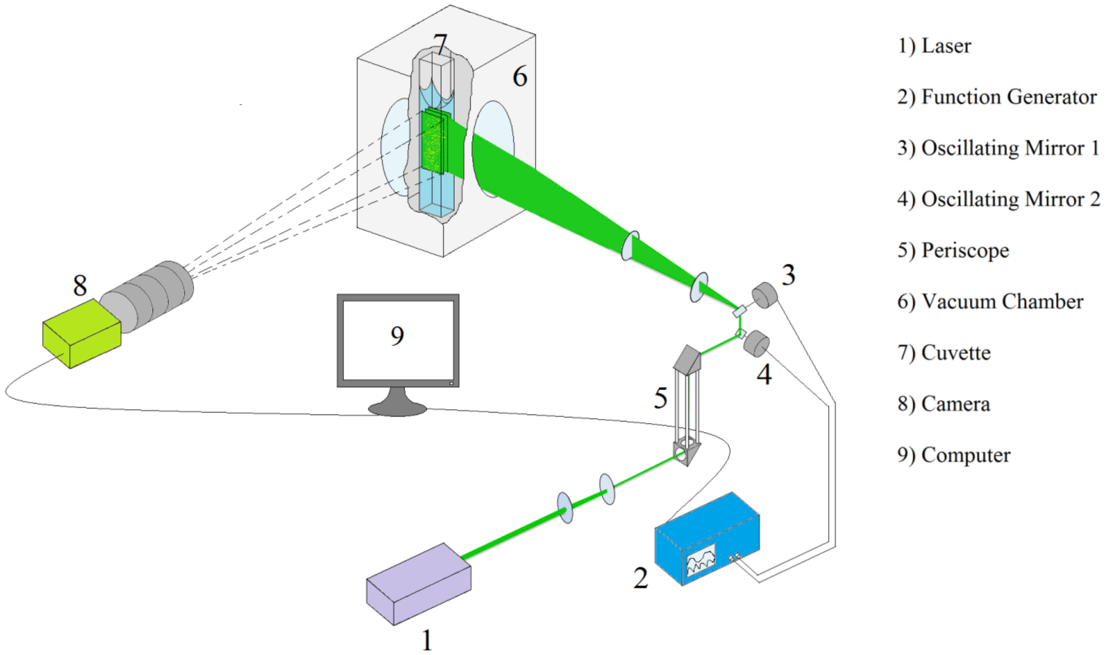

Fig. 1. Schematic diagram of the experimental setup, including the vacuum chamber, imaging, and illuminating systems

The imaging system includes a high-speed CCD camera (sp-5000M, JAI Inc) which is capable of collecting up to 134 frames per second. A 60 mm lens was attached in front of the camera using three lens extension tubes to focus the particles with a higher magnification. The field of view produced by the current optics covers approximately half of the height and the entire width of the cuvette. In an attempt to reduce the background noise during the data acquisition, a 530 nm filter was placed in front of the camera lens which only allows the fluorescent emission to be transmitted to the camera. The start of the image collection and also the number of images acquired for the 3D scanning PIV was controlled by custom software (National Instrument Labwindows CVI).

The illumination system including the laser and optics is represented schematically in Fig. 1. The beam from a continuous wave Nd:YAG laser passes through a converging lens with a focal length of 11 cm and is then expanded by a diverging lens of focal length 6.5 cm. This combination creates a narrower laser beam which makes it suitable for spreading over the majority of the galvanometer mirror area. After reflection through the periscope, the narrow beam strikes the galvanometer scanning mirrors. In order to make an extremely thin laser beam, two other converging lenses both having focal lengths of 11 mm were placed in front of the oscillating mirrors. The orientation of these two orthogonal mirrors determines the (y) and (z) position of the laser beam. The relatively fast oscillation of the upper mirror compared to the image collection speed causes the camera to see the beam as a laser sheet.

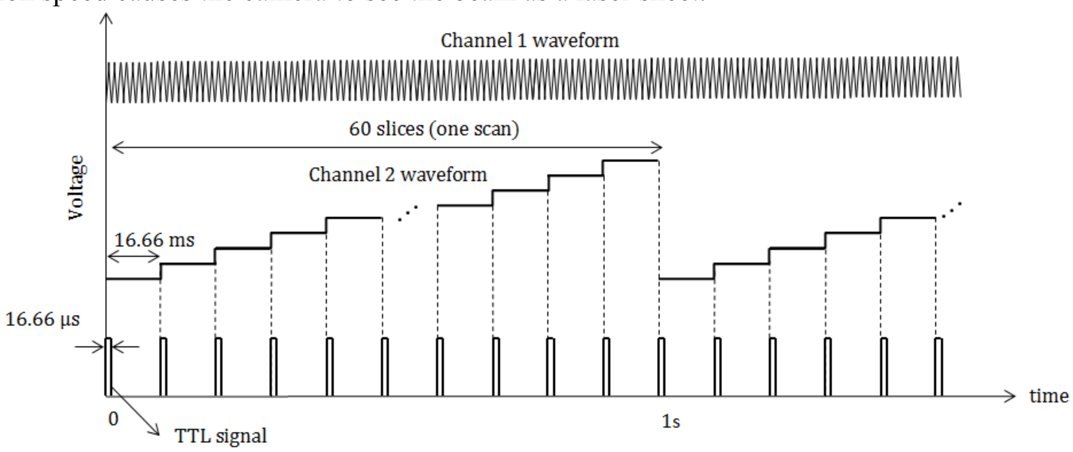

Fig. 2. Timing diagram of control signals to trigger the camera in sync with the moving mirrors.

The system employs a function generator to synchronize the laser sheet position with image capture. The function generator generates two output voltage signals which control the motion of the scanning mirrors. It also generates a TTL signal with respect to the signal in channel 2, which triggers image acquisition. The timing diagram for this experiment is displayed in Fig. 2. A triangle waveform which has a frequency of 6,250 Hz (channel 1 waveform in Fig. 2) controls the upper mirror position. Such a high frequency is required to move the laser beam up and down once per camera exposure time so that the camera can record the 2D image of each slice. A rising step waveform (channel 2 waveform in Fig. 2) controls the lower mirror and determines the location of the 2D slices within the 3D volume. For each sweep over the volume of interest, 60 slices were collected.

3 Data Processing

The concept of tomographic PIV [24] has been used to obtain the three components of the velocity field in the cuvette. The raw images which were captured during two individual volume scans were saved in a time series. In the first step, image pre-processing was performed on all images to reduce the background noise and improve the sharpness of the particle intensities. The regions where no flow existed were masked in this step as well. In the second step, each set of 60 images were stacked together to create a volume which contained the 3D position of particles from individual scans. These two reconstructed volumes were cross-correlated with commercial software (DaVis 8.2, LaVision GmbH) and the average displacement of particle ensembles over a set of voxels in the volume of interest was determined using a 3D algorithm. The correlation was conducted in three steps with different correlation window sizes of 32×32×32, 24×24×24, and 20×20×20 with 75 % overlap. The three-dimensional components of velocity can be calculated by knowing the time interval between the images and the actual size of pixels in millimeters. The former is a parameter adjusted by the user in the function generator and the latter can be obtained by calibration of the camera.

4 Results and Discussion

The technique presented has been applied to demonstrate the liquid flow pattern in evaporation of water at very low pressures. The operating pressure was set to the lowest possible (~200 Pa) in order to observe a more vigorous fluid motion. Fig. 3 represents the three-dimensional schematic of the cuvette filled with distilled and deionized water. The camera lens and lens extensions are configured such that only the particles in half of the width of the cuvette can be in focus. Therefore, the front half of the cuvette volume was selected to study the fluid motion. The small volume on the top of the swept volume was not processed and was masked due to an intense reflection of light from accumulated fluorescent particles on the interface.

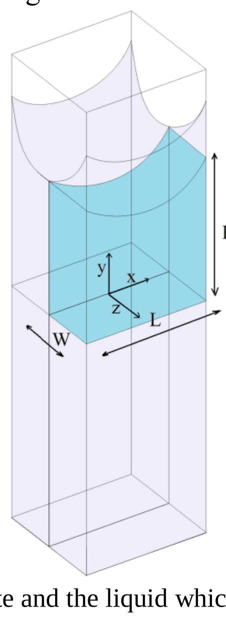

Fig. 3. Schematic representation of the cuvette and the liquid which forms a meniscus at the interface. The height, length, and the width of cuvette are 45 mm, 10 mm, and 4 mm. The approximate dimensions of the studied volume are $H \approx 10$ mm, $L = 10$ mm, and $W \approx 2$ mm.

The data obtained from the cross correlation step were only available at twelve planes through the volume. The number of planes at which the velocities are known depends on the size of the voxels in the image processing and increases as the voxels become smaller. The data was post-processed for display (MATLAB R2013a) and interpolated to obtain the velocity components at any point in the volume.

Fig. 4 shows the velocity magnitude in the liquid in terms of pixels per second which has been calculated by taking the square root of the sum of the squares of the x, y, and z components of velocity.

$$V = \sqrt{v_x^2 + v_y^2 + v_z^2} \tag{1}$$

where V (pixel/s) is the velocity magnitude and v_x (pixel/s), v_y (pixel/s), and v_z (pixel/s) are velocity components in the x, y and z directions, respectively. As can be seen from the figure, the highest velocity magnitude occurs in regions close to the interface.

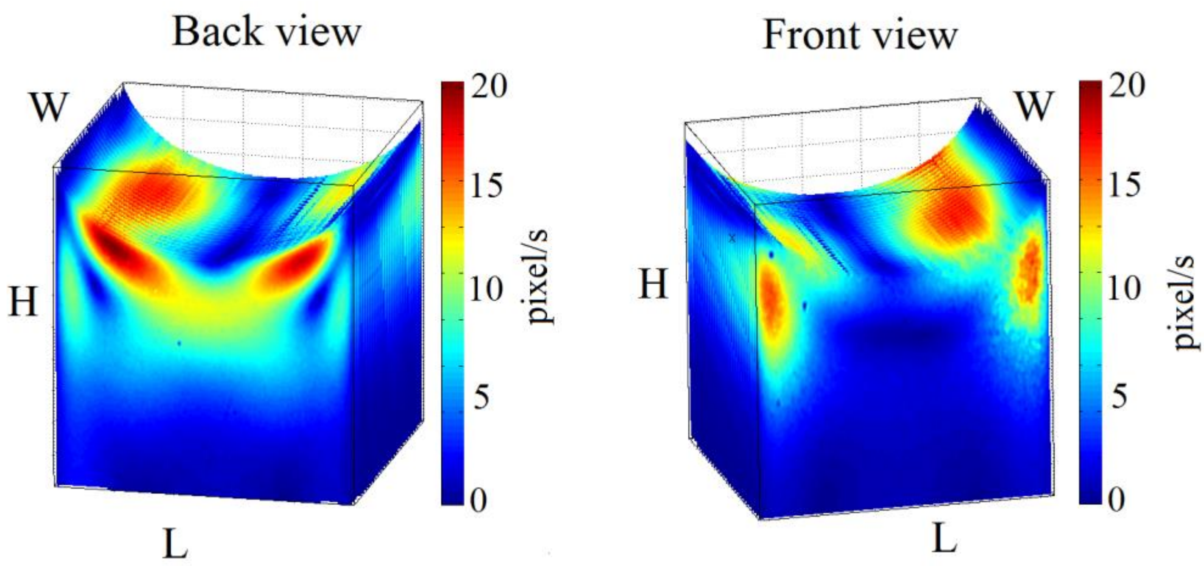

Fig. 4. Three-dimensional velocity magnitude in the liquid during an evaporation experiment

In order to see the flow direction, the two-dimensional and three-dimensional velocity arrows are shown in Fig. 5 and Fig. 6, respectively. In Fig. 6, only every 10th vector is shown and the background colour map highlights the magnitude of velocity. As shown in the figures, the water accelerates from the center to the wedges formed by the vertical walls and the surface meniscus. Then it turns back on the bulk flow along the wall and finally moves back to its initial position. This creates a doughnut shape convection pattern below the interface which transfers the energy from the warmer region (bottom) to the molecules at the interface, which are at a lower temperature due to the evaporative cooling effect.

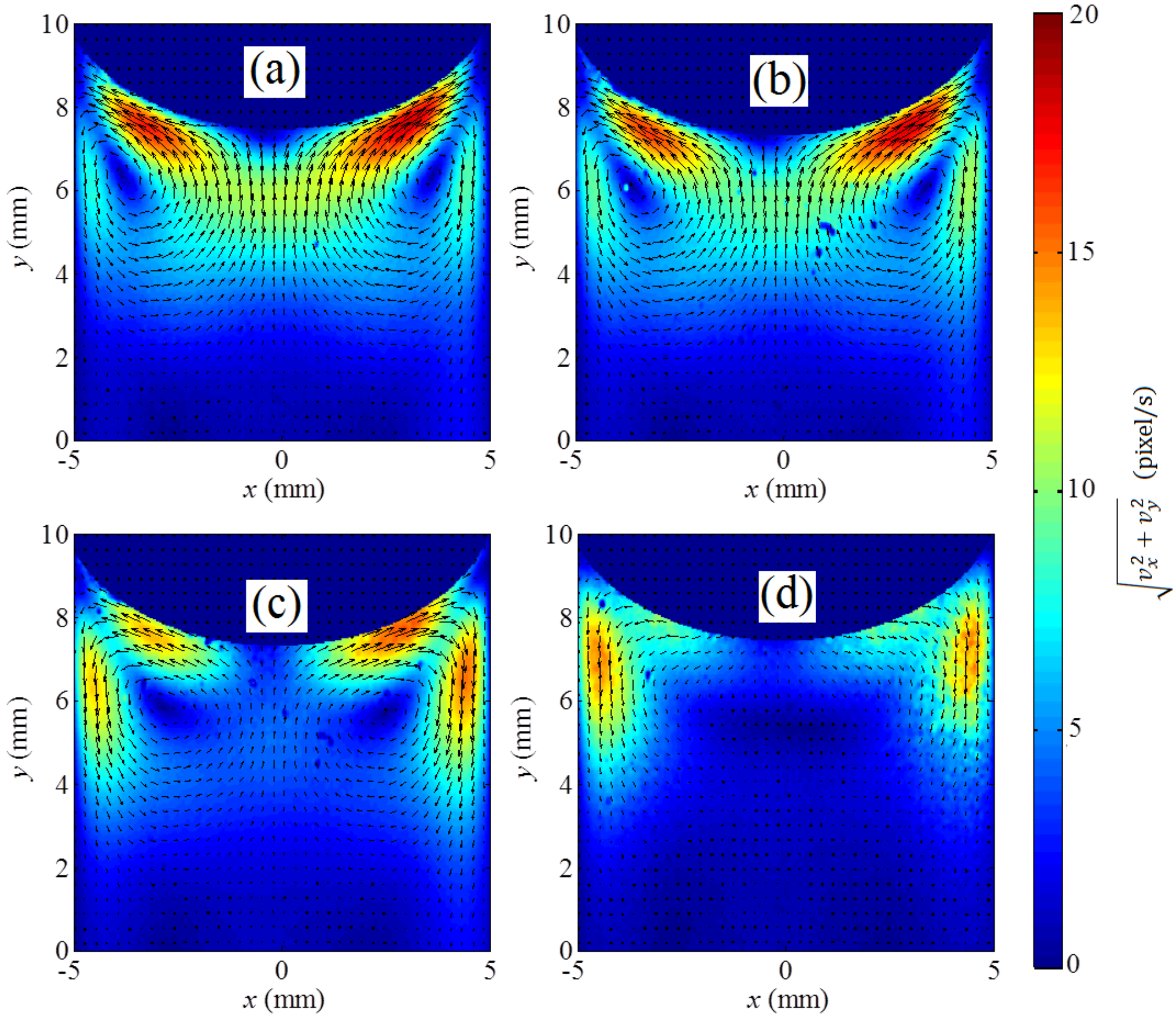

Fig. 5. The v_x and v_y components of the velocity field (every 10th vector shown) at four different plane positions (a) $z = 0$, (b) $z = W/3$, (c) $z = 2/3W$, and (d) $z = W$.

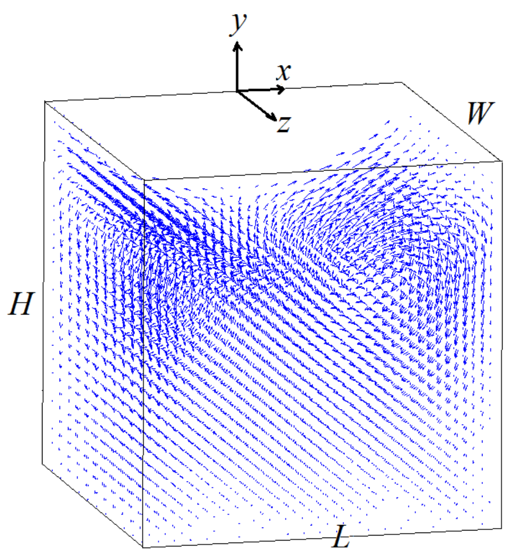

Fig. 6. A 3D representation of velocity arrows in the liquid.

Fig. 7 shows the two-dimensional vorticity in a colour map along with the velocity vector field (every 10th vector shown) on four planes in the volume. The figure reveals two large vortices on the scale of half of the cuvette width in the bulk liquid which rotate in opposite directions. Parts of two smaller vortices right below the interface are also observed which cannot be detected completely in this data plot.

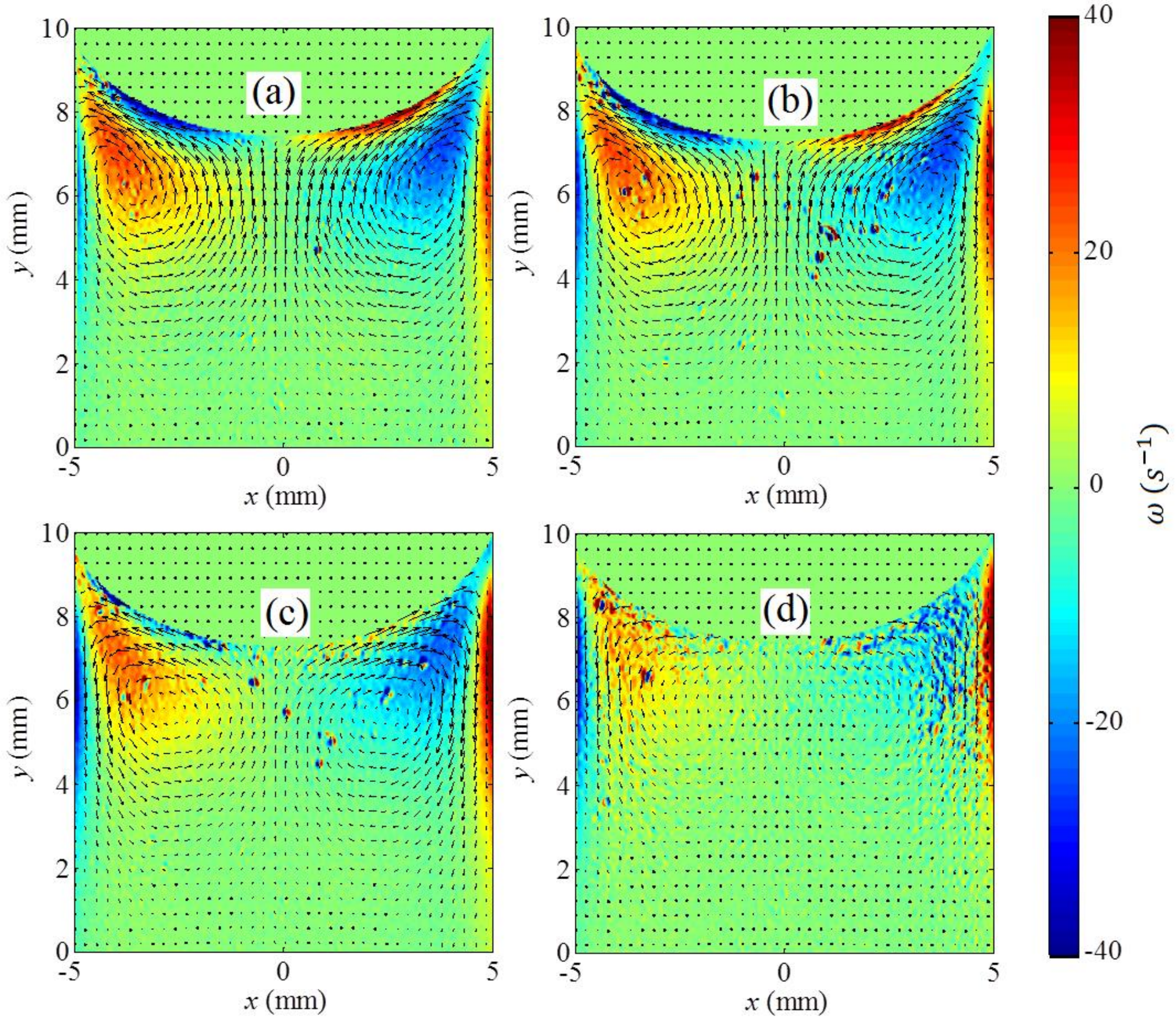

Fig. 7. The vector field (every 10th vector shown) mapped onto the two-dimensional vorticity field (ω) at four different widths, (a) z = 0, (b) z = W/3, (c) z = 2/3W, and (d) z = W.

Fig. 8 shows a magnified view of the vorticity field and the two-dimensional velocity vectors (every 3rd vector shown) in the top right corner of the cuvette. The display at a higher vector resolution shows that there is a separation point above the large vortex. This means that a portion of the flow moves toward the interface to form the small vortex in the top corner of the meniscus which has not been shown completely here. This separation point was not observed at the plane near the wall (Fig. 8 (d)). However, we cannot comment on the existence of such a point at this plane since a small part of the volume above is not captured in current data set. This is because of the strong curvature of the meniscus in this region and the need to mask out high reflections from the liquid interface.

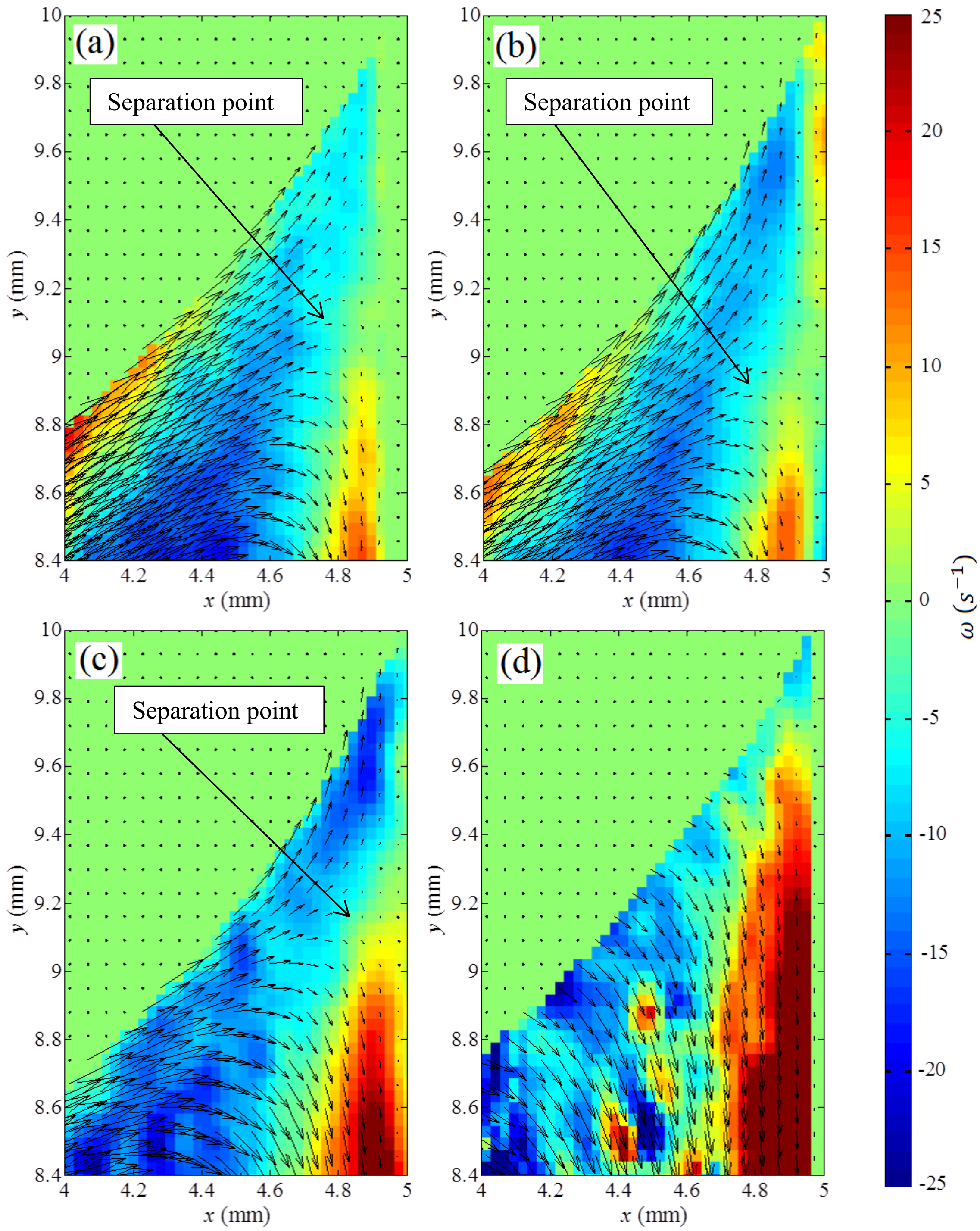

Fig. 8. Magnified view of vorticity field (ω) and velocity vectors (every 3rd vector shown) near the interface at four different widths showing the separation points, (a) z = 0, (b) $z = W/3$, (c) $z = 2/3W$, and (d) $z = W$.

Summary and Conclusion

In this paper, a 3D PIV method was utilized to visualize and quantify three components of velocity in an evaporating liquid in a rectangular cuvette. The 3D position of particles in the liquid was determined by scanning a laser sheet rapidly through a portion of the volume and imaging the slices with a CCD camera. Using commercial software (DaVis 8.2, LaVision GmbH), the sets of images were converted to volumes and the volumes were then cross correlated to give the displacements of particle ensembles in three dimensions and subsequently the three components of velocity in the volume of liquid. A strong vortex moving from the centerline to the walls was observed below the interface. The capability for 3D visualization and quantification of the flow in evaporating liquids will be helpful to get information about the direction and possible mechanisms of heat and mass transfer at the interface which are difficult to assess from previously reported experimental techniques.

Acknowledgments

The authors wish to thank Dr. Sina Ghaemi for his help in using the software and data processing. This research was funded by the Natural Sciences and Engineering Research Council (NSERC) of Canada, the Alberta Ingenuity Fund and the Canadian Foundation for Innovation (CFI). J. A. W. Elliott holds a Canada Research Chair in Thermodynamics.

References

[1] X. Pan, W. Jin, Y. Liu, and F. Ai, “Effect of surface tension-driven flow on BaB2O4 crystal growth from high temperature melt-solution,” *Cryst. Res. Technol.*, vol. 43, no. 2, pp. 152–156, 2008.

[2] T. Sutter, N. Kim, T. Kyu, and D. Golovaty, “ScienceDirect Crystal nucleation and motion in an undercooled binary solution,” pp. 1–5, 2015.

[3] R. Savino, N. di Francescantonio, R. Fortezza, and Y. Abe, “Heat pipes with binary mixtures and inverse Marangoni effects for microgravity applications,” *Acta Astronaut.*, vol. 61, no. 1–6, pp. 16–26, 2007.

[4] N. di Francescantonio, R. Savino, and Y. Abe, “New alcohol solutions for heat pipes: Marangoni effect and heat transfer enhancement,” *Int. J. Heat Mass Transf.*, vol. 51, no. 25–26, pp. 6199–6207, 2008.

[5] R. Savino and D. Paterna, “Marangoni effect and heat pipe dry-out,” *Phys. Fluids*, vol. 18, no. 11, pp. 2–6, 2006.

[6] Y. Cai and B. M. Z. Newby, “Marangoni flow-induced self-assembly of hexagonal and stripelike nanoparticle patterns,” *J. Am. Chem. Soc.*, vol. 130, no. 19, pp. 6076–6077, 2008.

[7] R. Bhardwaj, X. Fang, P. Somasundaran, and D. Attinger, “Self-assembly of colloidal particles from evaporating droplets: Role of DLVO interactions and proposition of a phase diagram,” *Langmuir*, vol. 26, no. 11, pp. 7833–7842, 2010.

[8] S. Lu, H. Fujii, and K. Nogi, “Marangoni convection and weld shape variations in Ar-O2 and Ar-CO2 shielded GTA welding,” *Mater. Sci. Eng. A*, vol. 380, no. 1, pp. 290–297, 2004.

[9] Y. Xiao-Hu and C. Xi, “Importance of Marangoni Convection in Laser Full-Penetration Welding,” *Chinese Phys. Lett.*, vol. 19, no. 6, pp. 788–790, 2002.

[10] F. L. a. Ganzevles and C. W. M. Van Der Geld, “Marangoni convection in binary drops in air cooled from below,” *Int. J. Heat Mass Transf.*, vol. 41, no. 10, pp. 1293–1301, 1998.

[11] H. Bénard, “Les tourbillons cellulaires dans une nappe liquide,” *Revue Générale des Sciences Pures et Appliquées.*, 11: pp. 1261-1271, 1901.

[12] M.J. Block, “Surface tension as the cause of Bénard cells and surface deformation in a liquid film,” *Nature* 178: pp. 650-651, 1956.

[13] J.R.A. Pearson, “On convection cells induced by surface tension,” *J. Fluid Mech.* 4: pp. 489-500, 1958.

[14] C. a Ward and F. Duan, “Turbulent transition of thermocapillary flow induced by water evaporation.,” *Phys. Rev. E. Stat. Nonlin. Soft Matter Phys.*, vol. 69, no. 5 Pt 2, p. 056308, 2004.

[15] H. Ghasemi and C. a. Ward, “Energy transport by thermocapillary convection during sessile-water-droplet evaporation,” *Phys. Rev. Lett.*, vol. 105, no. 13, pp. 1–4, 2010.

[16] X. Song and D. S. Nobes, “Experimental investigation of evaporation-induced convection in water using laser based measurement techniques,” *Exp. Therm. Fluid Sci.*, vol. 35, no. 6, pp. 910–919, 2011.

[17] A. Babaie, S. Madadkhani, B. Stoeber, A. Babaie, S. Madadkhani, and B. Stoeber, "Evaporation-driven low Reynolds number vortices in a cavity Evaporation-driven low Reynolds number vortices," vol. 033102, 2014.

[18] A. K. Thokchom, R. Swaminathan, and A. Singh, "Fluid Flow and Particle Dynamics Inside an Evaporating Droplet Containing Live Bacteria Displaying Chemotaxis," 2014.

[19] A. K. Thokchom, A. Gupta, P. J. Jaijus, and A. Singh, "Analysis of fluid flow and particle transport in evaporating droplets exposed to infrared heating," *Int. J. Heat Mass Transf.*, vol. 68, pp. 67–77, 2014.

[20] C. Buffone, K. Sefiane, and J. R. E. Christy, "Experimental investigation of self-induced thermocapillary convection for an evaporating meniscus in capillary tubes using micro-particle image velocimetry," *Phys. Fluids*, vol. 17, no. 5, pp. 1–18, 2005.

[21] H. K. Dhavaleswarapu, P. Chamarthy, S. V. Garimella, and J. Y. Murthy, "Experimental investigation of steady buoyant-thermocapillary convection near an evaporating meniscus," *Phys. Fluids*, vol. 19, no. 8, 2007.

[22] C. Minetti and C. Buffone, "Three-dimensional Marangoni cell in self-induced evaporating cooling unveiled by digital holographic microscopy," *Phys. Rev. E - Stat. Nonlinear, Soft Matter Phys.*, vol. 89, no. 1, pp. 1–6, 2014.

[23] Q. Gao, H. Wang, and G. Shen, "Review on development of volumetric particle image velocimetry," *Chinese Sci. Bull.*, vol. 58, no. 36, pp. 4541–4556, 2013.

[24] G. E. Elsinga, F. Scarano, B. Wieneke, and B. W. Van Oudheusden, "Tomographic particle image velocimetry," *Exp. Fluids*, vol. 41, no. 6, pp. 933–947, 2006.